

# Study of quark fragmentation in $e^+e^-$ annihilation at 29 GeV: Charged-particle multiplicity and single-particle rapidity distributions

M. Derrick, K. K. Gan,<sup>(a)</sup> P. Kooijman, J. S. Loos, B. Musgrave, L. E. Price,  
J. Repond, J. Schlereth, K. Sugano, J. M. Weiss,<sup>(b)</sup> and D. E. Wood<sup>(c)</sup>  
*Argonne National Laboratory, Argonne, Illinois 60439*

G. Baranko,<sup>(d)</sup> D. Blockus, B. Brabson, J. M. Brom, S. W. Gray,<sup>(e)</sup> C. Jung,  
H. Neal, H. Ogren, D. R. Rust, and M. Valdata-Nappi<sup>(f)</sup>  
*Indiana University, Bloomington, Indiana 47405*

C. Akerlof, G. Bonvicini, J. Chapman, D. Errede, N. Harnew,<sup>(g)</sup> P. Kesten,<sup>(h)</sup>  
D. I. Meyer, D. Nitz, A. A. Seidl,<sup>(c)</sup> R. Thun, T. Trinko,<sup>(c)</sup> and M. Willutzky  
*University of Michigan, Ann Arbor, Michigan 48109*

S. Abachi, P. Baringer, U. Mallik,<sup>(a)</sup> I. Beltrami,<sup>(i)</sup> B. G. Bylsma, R. DeBonte, F. Loeffler,  
E. H. Low, R. L. McIlwain, D. H. Miller, C. R. Ng, L. K. Rangan, and E. I. Shibata  
*Purdue University, West Lafayette, Indiana 47907*

B. Cork

*Lawrence Berkeley Laboratory, Berkeley, California 94720*

(Received 12 May 1986)

This paper presents the charged-particle multiplicity distributions for  $e^+e^-$  annihilation at  $\sqrt{s} = 29$  GeV measured in the High Resolution Spectrometer. The data, which correspond to an integrated luminosity of  $185 \text{ pb}^{-1}$ , were obtained at the SLAC  $e^+e^-$  storage ring PEP. The techniques used to correct the observed prong numbers are discussed. The multiplicity distribution of the charged particles has a mean value  $\langle n \rangle = 12.87 \pm 0.03 \pm 0.30$ , a dispersion  $D_2 = 3.67 \pm 0.02 \pm 0.18$ , and an  $f_2$  moment of  $0.60 \pm 0.02 \pm 0.18$ . Results are also presented for a two-jet sample selected with low sphericity and aplanarity. The charged-particle distributions are almost Poissonian and narrower than have been reported by other  $e^+e^-$  experiments in this energy range. The mean multiplicity increases with the event sphericity, and for the sample of threefold-symmetric three-jet events, a value of  $\langle n \rangle = 16.3 \pm 0.3 \pm 0.7$  is found. No correlation is observed between the multiplicities in the two hemispheres when the events are divided into two jets by a plane perpendicular to the thrust axis. This result is in contrast with the situation in soft hadronic collisions, where a strong forward-backward correlation is measured. For the single jets, a mean multiplicity of  $6.43 \pm 0.02 \pm 0.15$  and a dispersion value of  $D_2 = 2.55 \pm 0.02 \pm 0.13$  are found. These values give further support to the idea of independent jet fragmentation. The multiplicity distributions are well fit by the negative-binomial distribution. The semi-inclusive rapidity distributions are presented. Comparisons are made to the measurements of charged-particle multiplicities in hadron-hadron and lepton-nucleon collisions.

## INTRODUCTION

The measurement of multihadron production in  $e^+e^-$  annihilation is the simplest way to study the fragmentation of partons into hadrons since the parton-level processes are particularly simple. The center-of-mass energy of the hadronic system is clearly defined, and all of the incident energy contributes to the creation of particles, except for the well-known initial-state radiation. By contrast, in lepton-nucleon ( $l-N$ ) and hadron-hadron ( $h-h$ ) hard collisions, the initial state is a complex mixture of quarks and gluons, and the momentum distribution of the interacting constituents must be inferred from measurements on the final-state particles.

Detailed information is now available on global jet measures and single-particle distributions in  $e^+e^-$  annihilation into hadrons over a range of energies.<sup>1-6</sup> Because the jets can be so clearly identified in  $e^+e^-$  reactions in this energy range, and because they primarily originate from known mixtures of quarks, the results are important in validating our understanding of hadronization, as well as in comparing with the data from the  $pp$  and  $p\bar{p}$  colliders.

Apart from the known complications arising from the decay multiplicities of the leading mesons and the harder fragmentation functions that characterize final states involving heavy quarks, the hadronization process seems to be flavor independent.<sup>7</sup> The experimental situation with gluon jets is less clear although some data are now becoming available.<sup>8,9</sup>

At a phenomenological level, comparisons with other reactions, soft or hard, may reveal which features depend on constraints such as longitudinal phase space and which are intrinsic to quark fragmentation. In contrast with  $e^+e^-$  annihilation, which is a simple process at the parton level, soft-hadronic interactions are thought to represent a collective process yielding a forward and backward cone dominated by one leading particle, usually with the same quantum numbers as the initial beam or target, accompanied by a large number of soft particles produced in the collision. Thus, *a priori*, the mechanism of hadronization in the two reactions is expected to be quite different. Nevertheless, it has been shown<sup>10</sup> that the final states in hadron-hadron soft collisions, once the leading-particle effect has been subtracted, have some similarities to the  $e^+e^-$  data.

In a previous publication,<sup>1</sup> we reported results on global jet parameters and single-particle distributions. In this paper we present our results on charged-particle multiplicities and semi-inclusive single-particle rapidity distributions. These data provide strong constraints on the various fragmentation models that have been used to interpret the  $e^+e^-$  results, since the charged-particle multiplicities are particularly sensitive to the final steps in the hadronization. Comparison with similar hadronic data gives some significant insights into the nature of these reactions.

The approximate scaling of the charged-particle multiplicity distribution when expressed as a fraction of the mean, first suggested by Koba, Nielsen, and Olesen<sup>11</sup> and now known as KNO scaling, provides another link with hadronic data and with models that attempt to explain this phenomenon from general principles.

The analysis is based on data obtained with the High Resolution Spectrometer (HRS) operated at the SLAC  $e^+e^-$  storage ring (PEP) at a c.m. energy of 29 GeV. The data sample corresponds to a total integrated luminosity of  $185 \pm 5 \text{ pb}^{-1}$ . Comparisons are made with results from  $e^+e^-$  annihilation at the DESY storage ring PETRA, lepton-nucleon deep-inelastic scattering, and high-energy soft-hadronic reactions, in particular, the results observed in  $p\bar{p}$  interactions at the CERN  $S\bar{p}p$ S collider.

## APPARATUS

The HRS (Refs. 1 and 12), shown in Fig. 1, measures charged secondary particles over a solid angle of  $\sim 90\%$  of  $4\pi$ , covering the angular range  $|\cos\theta| < 0.9$ , where  $\theta$  is the angle with respect to the positron beam direction. The inner drift-chamber system, which is important for this analysis, consists of 15 cylindrical layers of drift cells; in seven of the layers, the wires are oriented axially; in the remaining eight layers they are at stereo angles of  $\pm 60$  mr. There are 2448 cells in this tracking chamber. At a radius of 1.98 m, the turning angle of the tracks is measured in a two-layer outer drift-chamber system.

The vacuum pipe of PEP and the inner cylinder of the drift-chamber vessel are made of beryllium so that there was typically 1.4% of a radiation length of material between the interaction point and the first tracking layer of

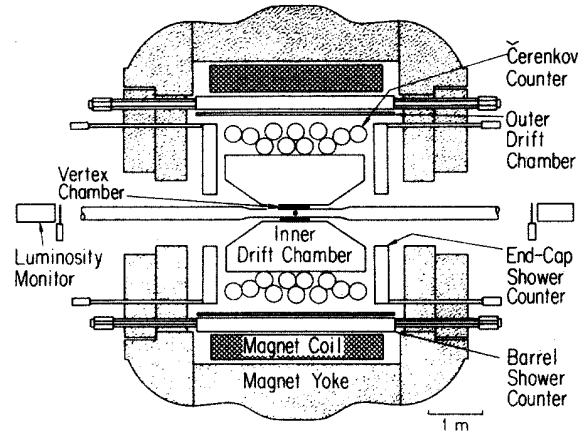


FIG. 1. Cross-section view of the High Resolution Spectrometer showing the inner and outer drift-chamber systems.

the detector. This thin front end, combined with the high solenoidal magnetic field of 1.62 T, means that additional tracks resulting from photon conversion are minimal.

The tracking system is surrounded by a set of barrel and end-cap shower counters consisting of lead-scintillator sandwiches with one layer of proportional wire chambers to measure the position of the showers. These counters are also located in the magnetic-field region. There are 40 modules in the barrel shower-counter system, each covering a  $9^\circ$  azimuthal segment, and extending to  $|\cos\theta| < 0.6$ . The energy resolution is given by  $(\sigma_E/E)^2 = (0.16)^2/E + (0.07)^2$  with  $E$  in GeV. The end-cap counters have 40 similar wedge-shaped modules that extend the coverage to  $|\cos\theta| \sim 0.9$ .

A four-layer vertex chamber is located inside the inner drift chamber. A set of Cerenkov counters are also located between the inner drift chamber and the outer tracking and shower-detection system. The signals from these detection elements are not used in the present analysis.

The detector was triggered by requiring the presence of either three or more charged tracks or two charged tracks, plus at least one signal in time with the beam crossing. Two neutral triggers were also used.<sup>1,12</sup>

## DEFINITION OF VARIABLES

The jet axis of an event is chosen as the direction of the thrust ( $T$ ) axis, where the thrust is defined as

$$T = \max_i \frac{\sum_j |p_L^j|}{\sum_j |p^j|}, \quad (1)$$

where  $p^i$  is the momentum of the  $i$ th track,  $p_L^i$  is the component of  $p^i$  along the  $T$  axis, and the sum extends over all charged tracks of the event. The jet axis may also be taken as that direction which minimizes the transverse momentum squared or sphericity ( $S$ ). The sphericity of the event is defined as

$$S = \frac{3}{2} \min \frac{\sum_i^n (p_T^i)^2}{\sum_i^n (p^i)^2}, \quad (2)$$

where  $p_T$  is the transverse momentum of the  $i$ th track with respect to a trial axis. The aplanarity ( $A$ ) is the normalized momentum square out of the event plane.

The mean center-of-mass energy ( $W$ ) of the event sample is 28.3 GeV, after accounting for initial-state radiation and the event-selection criteria.

The rapidity ( $Y$ ) is given by

$$Y = \frac{1}{2} \ln \left[ \frac{E + p_L}{E - p_L} \right], \quad (3)$$

where  $p_L$  is the momentum along the  $T$  axis. The positive  $Y$  direction is chosen along the positive  $z$  direction, which is the direction of the incident positron beam.

The multiplicity distribution for the charged particles is expressed in terms of a number of variables. The number of charged particles in any event is denoted by  $n$ . Charge conservation requires  $n$  to be even. The mean value of the multiplicity distribution is denoted by  $\langle n \rangle$ , while the shape of the distribution is characterized, in general, by the moments  $C_q = \langle n^q \rangle / \langle n \rangle^q$ , but is often parametrized by the dispersion  $D_2$ , where  $D_2^2 = \langle n^2 \rangle - \langle n \rangle^2$  and by the  $f_2$  moment defined as

$$f_2 = \langle n(n-1) \rangle - \langle n \rangle^2 = D_2^2 - \langle n \rangle.$$

The  $f_2$  moment is zero for a Poisson distribution. For negative prongs, the equivalent variables are denoted by  $\langle n_- \rangle$ ,  $D_2^-$ , and  $f_2^-$ . The events are divided into two individual jets by a plane perpendicular to the thrust axis, and the variables describing the properties of the individual jets are denoted by  $n$ ,  $\mathcal{D}_2$ , etc.

The multiplicity distributions for  $e^+e^-$  annihilation at different center-of-mass energies are often compared using then KNO form.<sup>11</sup> If  $Z$  is the scaled multiplicity  $n/\langle n \rangle$ , then KNO scaling says that all of the data can be represented by a universal function  $\psi(Z)$  given by

$$\psi(Z) = \langle n \rangle \frac{\sigma_n}{\sum \sigma_n}, \quad (4)$$

where  $\sigma_n$  is the cross section for producing an event with  $n$  charged particles.

The multiplicity distributions may also be compared to the negative-binomial (NB) distribution in the variable  $n$ :

$$P(n, \langle n \rangle, k) = \frac{k(k+1) \cdots (k+n-1)}{n!} \times \left[ \frac{\langle n \rangle/k}{1 + \langle n \rangle/k} \right]^n \left[ 1 + \frac{\langle n \rangle}{k} \right]^{-k}. \quad (5)$$

The position of this distribution is fixed by the mean value  $\langle n \rangle$  and its shape is determined by the parameter  $k$ . When  $k$  is an integer, the resulting shape is known as the generalized Bose-Einstein distribution and gives the distribution resulting from the superposition of  $k$  identical emitters. The variable  $k$  is related to  $\langle n \rangle$  and  $D_2$  by

$$\frac{D_2^2}{\langle n \rangle^2} = \frac{1}{\langle n \rangle} + \frac{1}{k}. \quad (6)$$

In the limit  $k \rightarrow \infty$ ,  $D_2^2 = \langle n \rangle$  and the NB expression (5) becomes a Poisson distribution:

$$P(n) = \frac{\langle n \rangle^n}{n!} e^{-\langle n \rangle}. \quad (7)$$

For  $k=1$ , the NB becomes the geometric distribution:

$$P(n) = \left[ \frac{\langle n \rangle}{1 + \langle n \rangle} \right]^n \frac{1}{1 + \langle n \rangle}, \quad (8)$$

which is the Bose-Einstein distribution for a single source.

Since the multiplicity distributions in KNO form have a sharp rise at low  $Z$ , followed by an exponential fall, fits to data have often used the gamma distribution (GD)

$$\psi(Z) = \frac{K^K}{(K-1)!} Z^{K-1} e^{-KZ}. \quad (9)$$

When  $K=1$ , the KNO distribution in this form is a simple exponential,  $\psi(Z) = e^{-Z}$ , and for  $K=2$  it becomes  $\psi(Z) = 4Ze^{-2Z}$ . The GD follows from the NB in the limit when  $\langle n \rangle \gg k$ .

If KNO scaling holds, then the  $k(K)$  values and the  $C_q$  moments of the multiplicity distribution will be energy independent.

Fits to the multiplicity distributions with the NB and GD give different numerical values for the  $k(K)$  parameters. They are approximately related by  $1/K = 1/k + 1/\langle n \rangle$ , so that for a Poisson distribution, with  $1/k = 0$ ,  $K \approx \langle n \rangle$ .

## EVENT SELECTION

To select the hadronic events for this study, some simple criteria were imposed on the data.

(1) The visible momentum ( $p_{\text{vis}}$ ) and the shower energy ( $E_{\text{sh}}$ ) had to exceed certain thresholds ( $p_{\text{vis}} > 7$  GeV/ $c$  or  $E_{\text{sh}} > 3$  GeV or  $p_{\text{vis}} + E_{\text{sh}} > 8$  GeV), where  $p_{\text{vis}}$  is the scalar sum of the charged-particle momenta and  $E_{\text{sh}}$  is the energy deposited in the shower counters.

(2) In order to suppress QED processes (such as Bhabha scattering or  $\tau$  pair production), beam-gas interactions, and cosmic-ray background, at least five charged prongs were required to come from a cylindrical fiducial volume, 3 cm radius in the  $x, y$  plane and  $\pm 15$  cm in  $z$ .

About one-half of the events passing the above selections were multihadron events resulting from one-photon annihilation. The remainder were mainly from two-photon processes, although a small contribution of six-prong  $\tau^+\tau^-$  events and beam-gas interactions were included.

To cleanly separate the one-photon annihilation events, to minimize geometrical losses of tracks making small angles with the beam, and to ensure well-reconstructed tracks, the following additional selections were applied.

(1)  $60^\circ < \theta_T < 120^\circ$ , where  $\theta_T$  is the polar angle of the thrust axis of the event determined from the charged particles. This restricts the event sample to be near the median plane of the detector where the track-reconstruction efficiency is high.

(2) Each charged track was required to have at least 60% of its potential hits in the central drift chamber, and have a polar angle  $\theta > 24^\circ$ . No track was required to reconstruct in the outer drift-chamber system.

(3)  $E_{\text{vis}} (= \sum_i |p^i| + \sum_i E^j) \geq 12 \text{ GeV}$ , where  $\sum_i |p^i|$  is the scalar sum of the momenta for all accepted charged tracks.  $\sum_i E^j$  is the energy deposited in the shower counters summed over all of the modules in the barrel and end-cap systems that had  $E^j > 200 \text{ MeV}$ . This cut discards noise signals as well as minimizing the contribution from most of the charged particles.

(4) Six-prong  $\tau$  events were rejected by requiring that the three-particle invariant mass of each jet be greater than the  $\tau$  mass. Pion masses were assigned to the observed tracks.

These selections gave a data sample of 29 649 events.

In addition to this inclusive data set, a sample of two-jet events was selected using the sphericity ( $S$ ) and aplanarity ( $A$ ) variables, where the  $S$  and  $A$  values were set by the eigenvalues of the momentum tensor. As in our previous study,<sup>1</sup> the collimated ( $S < 0.25$ ) and planar ( $A < 0.10$ ) events are called two jet. These additional cuts, which exclude the events with hard-gluon radiation, reduce the data sample to 24 553 events. This data set, excluding the events with hard-gluon radiation, may be more appropriate for comparison with the results from hadronic beam jets.

### DETECTOR SIMULATION

Corrections for acceptance and inefficiencies of the detector, as well as for the smearing introduced by measuring errors, were made using a Monte Carlo (MC) simulation of the experiment. The event simulation proceeded in two steps: (1) Generation of  $q\bar{q}$  and  $q\bar{q}g$  events in first-order QCD (Ref. 13); (2) evolution into hadrons using Field and Feynman<sup>14</sup> fragmentation functions.

The particles were propagated through the detector, generating hits in the tracking chambers and signals in the electromagnetic calorimeters. Energy loss, photon conversion, multiple scattering, particle decay, and the intrinsic resolution of the detector elements were taken into account. The resulting signals were then passed through the same track-reconstruction and selection program as was used for the real data.

The overall event-detection efficiency was measured by comparing the number of reconstructed MC events satisfying the selection criteria to the number of generated events. For events surviving the polar angle cut on the thrust axis, the detection efficiency is  $\sim 85\%$ . This efficiency estimate is only slightly dependent on the details of the MC model. The remaining background is less than 5% and comes mainly from two-photon processes and  $\tau^+\tau^-$  events. The cuts were tuned, using the MC simulation, to minimize biases that could distort the distributions reported in this paper.

Since this study reports charged-particle multiplicities, it depends critically on a good understanding of the response of the drift-chamber system to the charged prongs. After the charged tracking had been completed, a final cleanup was done. This operation eliminated three

types of spurious tracks: (1) Tracks considered to be spurious due to low quality; (2) tracks that appeared to be duplicates of other, better tracks; (3) tracks that appeared to be made up of fragments of other tracks. In the initial track finding and reconstruction, the track candidates change and develop as the reconstruction process proceeds, and the looser cuts help to define better orbits. The final cleanup step allowed rather tighter cuts on track quality than was possible in the earlier stages. In addition, the techniques used to reject duplicate tracks are more efficient when the overall event is complete.

The procedures were tuned using data; initially the sample of two-prong Bhabha scattering events and later, the  $D^{*+} \rightarrow D^0 \pi^+$  decays, which are cleanly tagged by the excellent spectrometer resolution and the limited kinematics available to the bachelor pion.<sup>15</sup> These measurements, as well as our studies<sup>16</sup> of other low-multiplicity final states such as  $e^+e^-$ ,  $\mu^+\mu^-$ , and  $\tau^+\tau^-$ , show that the track-reconstruction efficiency for isolated tracks is greater than 99% and is uniform for  $|\cos\theta| < 0.8$ .

A further test was made using the multihadron events generated by the MC program. This study was done statistically, using the large MC event sample, by comparing "tracking efficiency" evaluated in two different ways. The first method simply calculated the number of charged tracks reconstructed versus the number originally generated in the two-dimensional space of  $|\mathbf{p}|$  vs  $\cos\theta$ . Here  $|\mathbf{p}|$  is the absolute three-momentum and  $\theta$  is the polar angle of the orbit tangent with respect to the beamline at the point of closest approach. The second method involved the calculation of these same quantities but with

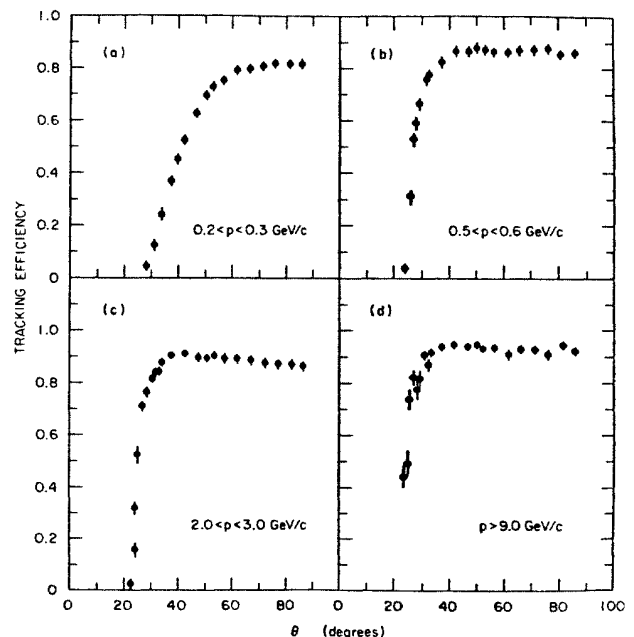


FIG. 2. Track-reconstruction efficiencies as a function of  $\theta$ , the polar angle with respect to the  $e^+e^-$  beam direction. Four different momentum intervals are shown: (a)  $0.2 < p < 0.3 \text{ GeV}/c$ ; (b)  $0.5 < p < 0.6 \text{ GeV}/c$ ; (c)  $2.0 < p < 3.0 \text{ GeV}/c$ ; and (d)  $p > 9 \text{ GeV}/c$ .

the additional constraint that the reconstructed orbits survived a mapping back onto the original MC-generated tracks via the list of drift-chamber coordinates employed in the track fitting and simulation. The two methods yielded good agreement only after the final track cleanup operations. The accidental loss of real tracks was small.

Typical results of these studies are shown in Fig. 2, which gives the reconstruction efficiency for different momentum intervals as a function of  $\theta$ . For  $p > 2$  GeV/c, the efficiency is about 90%. For  $\theta > 30^\circ$  and  $p > 200$  MeV/c, the track-reconstruction efficiency is 80% or better, and varies slowly with angle. Lower-momentum tracks are not well reconstructed for any dip angle because of the high magnetic field of the spectrometer. The minimum momentum for detecting tracks with good efficiency is about 200 MeV/c.

The track definitions include most of the charged particles from  $K_S^0$  and  $\Lambda$  decays, but exclude essentially all particles from  $K_L^0$  decays.

### CORRECTIONS TO THE CHARGED-PARTICLE MULTIPLICITIES

The distribution of the observed multiplicity ( $m$ ) for each true multiplicity ( $n$ ) was determined from the MC simulation. The histograms of Fig. 3 illustrate the results

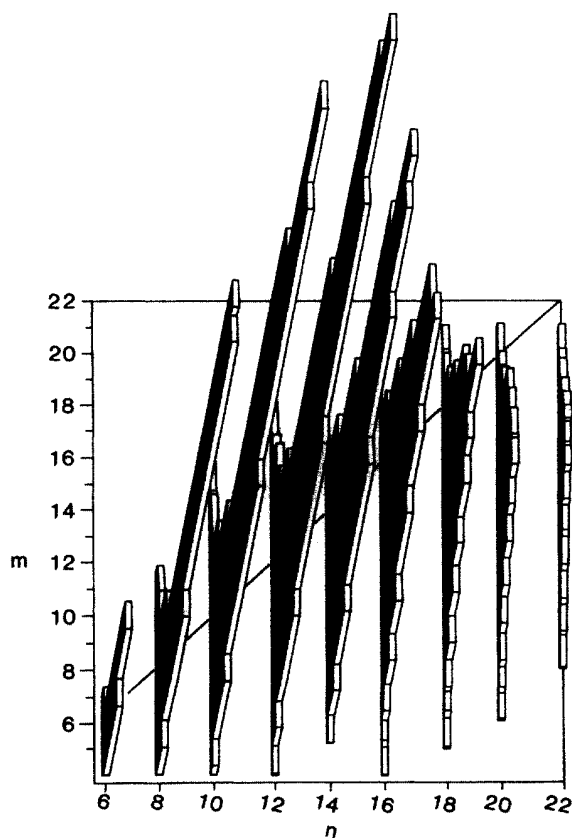


FIG. 3. Generated and reconstructed charged-particle multiplicity distribution according to the Monte Carlo study. The number of generated tracks in an event is  $n$ , whereas  $m$  is the number of tracks reconstructed.

of one such study. In this figure the projection on the  $n$  axis gives the assumed original multiplicity distribution and the projection on the  $m$  axis shows the smeared distribution that would be measured by the experiment. For the lower multiplicities ( $n \leq 10$ ) the observed prong number distribution is only slightly shifted from that generated. For the events generated with higher multiplicities, the smearing is more pronounced and in addition, the distribution are systematically shifted to lower observed values.

The number of events with 0, 2, and 4 charged particles, which were removed in the event selection, have been estimated in two ways: from the MC simulation and from the data themselves. In the MC event generator, the Feynman and Field independent-fragmentation model and the Lund string model give predictions for the low-multiplicity events that differ by about a factor of 2. The data themselves were therefore used, assuming independent fragmentation of the two jets that characterize most of the events. This is a good approximation as we discuss later. If  $p_i$  is the probability of a quark to fragment into a jet with  $i$  charged particles, the number of events with  $n = 2$  and  $n = 4$  are

$$N_2 = 2N(p_1^2 + 2p_0p_2), \quad (10)$$

$$N_4 = 2N(p_2^2 + 2p_1p_3 + 2p_0p_4),$$

where  $N$  is the total number of events each containing two jets. The factor of 2 arises since charge conservation only allows half of the  $p_i$ 's to be realized. The values of  $p_0 \cdots p_4$  were measured from the high-multiplicity events that are unaffected by the cut at  $m = 5$ .

A probability matrix  $P$  can be defined with elements  $P_{mn}$  giving the probability that a true  $n$  prong event will be observed as an  $m$  prong event after radiative corrections, the detector simulation, the acceptance cuts, and the event reconstruction procedures. Charge conservation requires that every second column in the  $P$  matrix be zero. If  $O$  is the observed multiplicity distribution with  $N_m^O$  the number of events with  $m$  tracks and similarly if  $T$  is the true multiplicity distribution with  $N_n^T$  the number of events with  $n$  tracks, then the true multiplicity distribution can, in principle, be calculated from the equation

$$O = PT. \quad (11)$$

Equation (11) can be solved by minimizing the quantity  $\chi^2$ , where

$$\chi^2 = \sum_m \frac{\left[ N_m^O - \sum_n P_{mn} N_n^T \right]^2}{\sigma_m^2} \quad (12)$$

and  $\sigma_m$  is the error on  $N_m^O$ .

This method was reliable in determining  $\langle n \rangle$ , but was numerically unstable in the determination of the shape of the multiplicity, since nearby multiplicity channels are highly correlated. It was therefore only used to measure  $\langle n \rangle$ . The mean multiplicity was also measured by weighting each track in the event with the track-reconstruction efficiency, as a function of the emission angles and momenta.

To obtain the shape of the multiplicity distribution we use the fact that the MC simulation is a good representation of the final result and can be used to construct a matrix  $\mathbf{M}$  from  $\mathbf{T}$  and the probability matrix  $\mathbf{P}$ . The matrix elements  $M_{mn} = P_{mn} N_n^T$  give the number of events that have  $n$  true tracks and  $m$  observed tracks. After normalization row by row the true multiplicity distribution was calculated from the equations

$$N_n^T = \sum_m M_{nm} N_m^0. \quad (13a)$$

The values of the matrix elements  $M_{mn}$  are dependent on the track- and event-selection cuts. The analysis was repeated using different definitions of an acceptable track and the results were found to be insensitive to the exact selections, provided that the MC-generated events were treated in the same way.

This technique does not critically depend on having a good initial representation of the multiplicity distribution since the procedure can be iterated. In practice, this was not necessary since the multiplicity distribution of the events generated by the MC program was close to our measurements.

By comparing the results obtained using these different approaches, from the uncertainty in the estimate of the low multiplicities and from the technique used to unfold the observed distribution, we assign systematic errors of  $\pm 5\%$  to the measurement of dispersion  $D_2$ , and  $\pm 2.4\%$  to that of  $\langle n \rangle$ .

## RESULTS

### Energy dependence of the mean charged multiplicity

The analyses gave  $\langle n \rangle = 12.87 \pm 0.03 \pm 0.30$ , where the first error is statistical and the second systematic. The charged particles from heavy-meson ( $K_s^0, D, F, \dots$ ) and baryon ( $\Lambda, \Sigma, \Lambda_c, \dots$ ) decays are included in these values. Our measured multiplicities of  $\langle n \rangle_{K^0} = 1.44 \pm 0.05 \pm 0.09$  (Ref. 17) and  $\langle n \rangle_{\Lambda} = 0.220 \pm 0.007 \pm 0.022$  (Ref. 18) reduces  $\langle n \rangle$  to  $11.34 \pm 0.03 \pm 0.3$  if the charged particles from these decays are omitted.

The dependence of  $\langle n \rangle$  on the c.m. energy for  $e^+e^-$  annihilation is shown in Fig. 4, where we compare our result with data from other experiments.<sup>2-6,19</sup> Various parametrizations for the  $W$  variation of  $\langle n \rangle$  have been proposed; phase spacelike production, as first suggested by Fermi,<sup>20</sup> predicts

$$\langle n \rangle = \alpha W^{1/2}. \quad (13b)$$

The Feynman scaling hypothesis,<sup>21</sup> plus a constant plateau in rapidity, leads to a logarithmic evolution:

$$\langle n \rangle = a + b \ln(W^2). \quad (14)$$

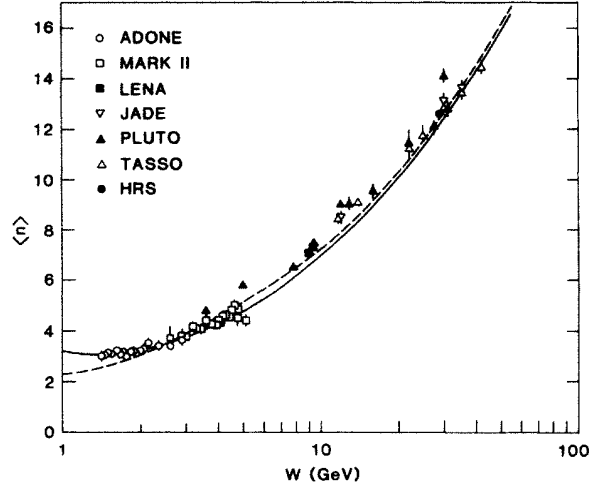


FIG. 4. Mean charged multiplicity in  $e^+e^-$  annihilation as a function of center-of-mass energy  $W$ . The solid (dashed) curve shows a  $a + b \ln(W^2) + c \ln^2(W^2)$  ( $a + b \ln(W^2)$ ) variation with the values of the constants given in the text.

However, fits to  $pp$  data up to CERN ISR energies show a faster growth that can be fit by

$$\langle n \rangle = a + b \ln(W^2) + c \ln^2(W^2). \quad (15)$$

This is consistent with the observed rise in the height of the rapidity plateau as the energy is increased.

A form

$$\langle n \rangle = a + b \exp\{c[\ln(W/Q_0)]^{1/2}\} \quad (16)$$

results from a QCD calculation for the evolution of partons in leading-logarithmic approximation.<sup>22,23</sup> In this expression  $Q_0$  is a constant related to the  $\Lambda$  parameter of QCD.

All of the above functions, except the simple  $a + b \ln(W^2)$  form, describe the data reasonably well. For example, the functions (13b) and (15) are drawn in Fig. 4, using the parameters  $\alpha = 2.3$  (dashed curve) and  $a = 3.33$ ,  $b = -0.4$ ,  $c = 0.26$  (solid curve).

Figure 5(a) compares the  $\langle n \rangle$  measurement in  $e^+e^-$  annihilation with those for  $h-h$  and  $l-N$  interactions.<sup>24-29</sup> The qualitative agreement between  $\langle n \rangle$  for  $\bar{p}p$  and  $e^+e^-$  annihilation channels hints at a phase-space dominance. However, there are significant differences in the absolute values of  $\langle n \rangle$  for  $e^+e^-$ ,  $h-h$ , and  $l-N$  interactions. These differences can be accounted for, only in part, by the cross section for heavy-quark ( $c, b$ ) production, which is almost one-half of the  $e^+e^-$  annihilation, about 10% in  $l-N$ , and very small in  $h-h$  interactions. Another obvious difference is the production of  $K_s^0$  and  $\Lambda$  particles, whose charged decay prongs are included in the  $e^+e^-$  data but not in the  $l-N$  and  $h-h$  data.

Guided by the similarities of  $\langle n \rangle$  in  $e^+e^-$  and  $\bar{p}p$  annihilation,<sup>29</sup> the observed regularities can be qualitatively understood.

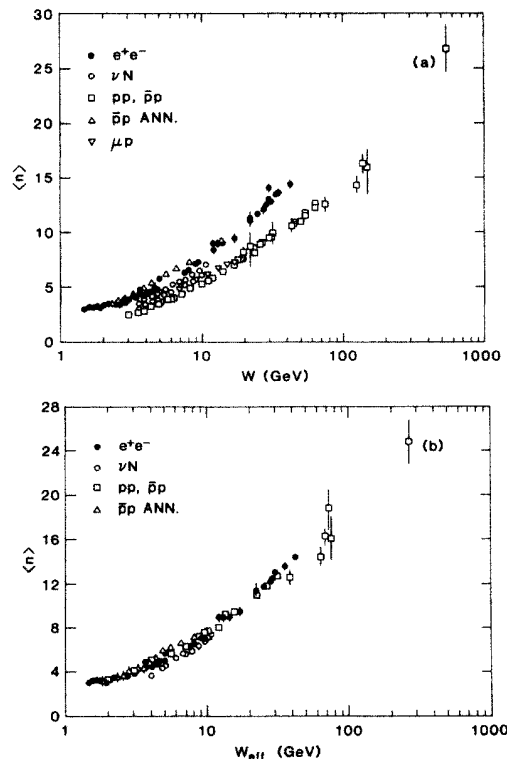


FIG. 5. Comparison of mean charged multiplicity measured in  $e^+e^-$  annihilation, hadronic collisions, and lepton-nucleon reactions: (a) using c.m. energy  $W$ , (b) using effective c.m. energy  $W_{\text{eff}}$  (see text).

(a) The presence of one or two nucleons in the final state of  $h-h$  and  $l-N$  reactions reduces the energy available for particle production and thus tends to decrease  $\langle n \rangle$  with respect to  $e^+e^-$  and  $\bar{p}p$  annihilations.

(b) The presence of leading particles in  $h-h$  reactions tends to decrease  $\langle n \rangle$ .

(c) The presence of a diffractive component in hadronic reactions, not always completely subtracted in the results, decreases  $\langle n \rangle$  and increases  $D_2$ .

(d) A higher absolute value of the total hadronic charge in  $\nu p$  scattering yields a higher  $\langle n \rangle$  for the low c.m. energies that characterizes these data.

In Fig. 5(b) we compare  $\langle n \rangle$  measurements in  $e^+e^-$  and  $\bar{p}p$  annihilation with the multiplicities in  $l-N$  interactions (forward cone) and  $pp$  reactions taken, in the latter case, as the energy available for hadronization ( $W_{\text{eff}}$ ) the c.m. energy  $W$  divided by two. These simple selections account for the main differences between the three reactions, and with these assumptions, the multiplicities follow a universal curve, as shown in Fig. 5(b), regardless of the reaction involved.

Although quantitative comparisons of multiplicities in lepton- and hadron-induced processes have been made using the energy available for particle production as the dependent variable and discarding the leading particles,<sup>10</sup> it is difficult to carry out such studies in an unambiguous way. As we discuss later, the detailed properties of  $e^+e^-$  and hadronic multiplicity distributions are quite different.

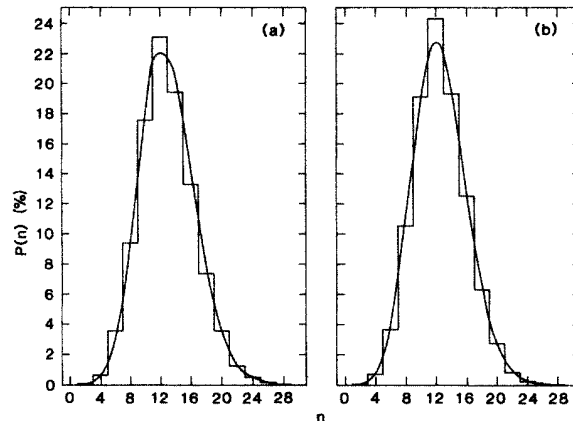


FIG. 6. Charged-particle multiplicity measurements (histogram) compared to the line that connects points on a Poisson distribution with the same mean value: (a) inclusive data sample, (b) two-jet data sample.

### SHAPE OF THE MULTIPLICITY DISTRIBUTION

The charged-particle multiplicities are listed as percentages in Table I, along with the results for the data set with the two-jet selection  $A < 0.1$  and  $S < 0.25$ . The first error gives the statistical uncertainty and the second the estimated systematic error. For the higher-multiplicity values, the smearing introduced by the granularity of the tracking chamber dominates the systematic error; for the low multiplicities, the cut at  $m=5$  gives the main source of uncertainty. The selection of two-jet events has only a small overall effect on the multiplicity values, although the population of the higher  $n$  values are reduced. This is expected as the events with hard-gluon radiation preferentially populate the higher multiplicities.

These data are shown in Fig. 6 for the unselected data set [Fig. 6(a)] and for the data with a two-jet selection [Fig. 6(b)]. The curves join points calculated from twice the Poisson distribution of Eq. (7) normalized to two, with

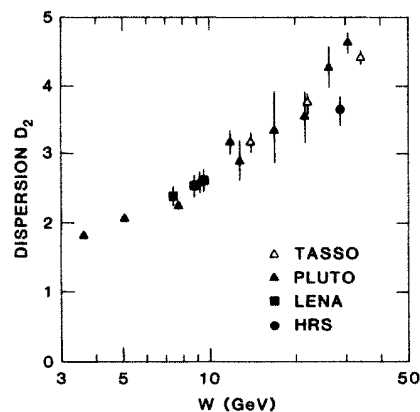


FIG. 7. Dispersion  $D_2$  of the charged-particle multiplicity distributions in  $e^+e^-$  annihilation as a function of center-of-mass energy  $W$ . Only the statistical errors are shown except for the HRS point, which also includes the systematic uncertainties.

TABLE I. Charged-particle multiplicity distributions. Values in percentages.

$n$	Inclusive sample		Two-jet sample	
	Whole event	Single jet	Whole event	Single jet
0		$0.04 \pm 0.02 \pm 0.02$		$0.04 \pm 0.02 \pm 0.02$
1		$1.48 \pm 0.04 \pm 0.70$		$1.54 \pm 0.04 \pm 0.73$
2	$0.05 \pm 0.02 \pm 0.02$	$3.42 \pm 0.09 \pm 1.13$	$0.05 \pm 0.02 \pm 0.02$	$3.49 \pm 0.09 \pm 1.13$
3		$6.48 \pm 0.15 \pm 0.30$		$6.89 \pm 0.15 \pm 0.32$
4	$0.63 \pm 0.05 \pm 0.20$	$11.44 \pm 0.20 \pm 0.50$	$0.69 \pm 0.06 \pm 0.22$	$12.09 \pm 0.20 \pm 0.53$
5		$15.32 \pm 0.23 \pm 0.67$		$16.15 \pm 0.24 \pm 0.71$
6	$3.56 \pm 0.10 \pm 0.20$	$15.89 \pm 0.23 \pm 0.69$	$3.66 \pm 0.10 \pm 0.21$	$16.38 \pm 0.24 \pm 0.71$
7		$14.34 \pm 0.22 \pm 0.62$		$14.37 \pm 0.22 \pm 0.62$
8	$9.43 \pm 0.20 \pm 0.41$	$11.61 \pm 0.20 \pm 0.50$	$10.48 \pm 0.23 \pm 0.45$	$11.38 \pm 0.20 \pm 0.49$
9		$8.33 \pm 0.17 \pm 0.37$		$7.92 \pm 0.16 \pm 0.35$
10	$17.54 \pm 0.24 \pm 0.76$	$5.14 \pm 0.13 \pm 0.23$	$19.07 \pm 0.28 \pm 0.82$	$4.61 \pm 0.12 \pm 0.21$
11		$3.15 \pm 0.10 \pm 0.15$		$2.72 \pm 0.09 \pm 0.13$
12	$23.12 \pm 0.27 \pm 1.00$	$1.65 \pm 0.07 \pm 0.10$	$24.21 \pm 0.29 \pm 1.05$	$1.22 \pm 0.05 \pm 0.07$
13		$1.01 \pm 0.06 \pm 0.05$		$0.78 \pm 0.05 \pm 0.04$
14	$19.43 \pm 0.25 \pm 0.84$	$0.42 \pm 0.04 \pm 0.04$	$19.21 \pm 0.25 \pm 0.83$	$0.27 \pm 0.03 \pm 0.03$
15		$0.17 \pm 0.02 \pm 0.02$		$0.08 \pm 0.01 \pm 0.02$
16	$13.32 \pm 0.20 \pm 0.58$	$0.07 \pm 0.02 \pm 0.02$	$12.42 \pm 0.18 \pm 0.54$	$0.04 \pm 0.01 \pm 0.01$
17		$0.03 \pm 0.01 \pm 0.01$		$0.02 \pm 0.01 \pm 0.01$
18	$7.38 \pm 0.16 \pm 0.36$	$0.01 \pm 0.01 \pm 0.01$	$6.29 \pm 0.12 \pm 0.31$	$0.01 \pm 0.01 \pm 0.01$
19				
20	$3.59 \pm 0.11 \pm 0.25$		$2.75 \pm 0.09 \pm 0.19$	
21				
22	$1.24 \pm 0.07 \pm 0.14$		$0.84 \pm 0.04 \pm 0.10$	
23				
24	$0.50 \pm 0.04 \pm 0.08$		$0.23 \pm 0.02 \pm 0.04$	
25				
26	$0.17 \pm 0.03 \pm 0.04$		$0.09 \pm 0.02 \pm 0.01$	
27				
28	$0.04 \pm 0.02 \pm 0.01$		$0.01 \pm 0.01 \pm 0.01$	

the average values of  $\langle n \rangle = 12.87$  and  $\langle n \rangle = 12.53$ , respectively. The data are remarkably close to this simple shape which could be expected for the random emission of single particles. This is certainly an oversimplification since it is known that resonances and heavy-quark states are important components in the final hadronic system,<sup>30</sup> and so many of the observed tracks are secondary decay products of such systems.

The properties of the multiplicity distribution are listed in Table II. The  $f_2$  moments are small, positive for the inclusive data and negative for the two-jet sample, and consistent with the small deviations seen between the data histograms and the Poisson curves in Fig. 6. The value of

the dispersion  $D_2$  of  $3.67 \pm 0.02 \pm 0.18$  is lower than the values previously reported for inclusive  $e^+e^-$  annihilation, as seen in Fig. 7, although not outside of the range defined by the systematic uncertainties of the other experiments. The HRS data points in Fig. 7 include both statistical and systematic errors, whereas for the other points only the statistical errors are shown.

A more detailed shape comparison, using the KNO form, is given in Fig. 8, where the present measurements are compared to results from the TASSO experiment<sup>4</sup> at  $W$  values of 14, 22, and 34 GeV. The errors shown are statistical. The present measurements exhibit a systematically narrower distribution. The statistical errors on the

TABLE II. Properties of the multiplicity distributions.

Variable	Inclusive sample		Two-jet sample	
	Whole event	Single jet	Whole event	Single jet
$\langle n \rangle$	$12.87 \pm 0.03 \pm 0.30$	$6.43 \pm 0.02 \pm 0.15$	$12.53 \pm 0.03 \pm 0.30$	$6.26 \pm 0.02 \pm 0.15$
$D_2$	$3.67 \pm 0.02 \pm 0.18$	$2.55 \pm 0.02 \pm 0.13$	$3.48 \pm 0.02 \pm 0.17$	$2.45 \pm 0.02 \pm 0.12$
$f_2$	$0.60 \pm 0.02 \pm 0.18$	$-0.07 \pm 0.02 \pm 0.13$	$-0.42 \pm 0.02 \pm 0.17$	$-0.26 \pm 0.02 \pm 0.13$
$\langle n \rangle / D_2$	$3.51 \pm 0.18$	$2.52 \pm 0.13$	$3.60 \pm 0.18$	$2.56 \pm 0.13$
K GD fit	12.3	7.11	13.3	7.49
$1/k$ NB fit	$3.9 \times 10^{-3}$	$1.4 \times 10^{-4}$	$4.3 \times 10^{-5}$	$1.4 \times 10^{-4}$



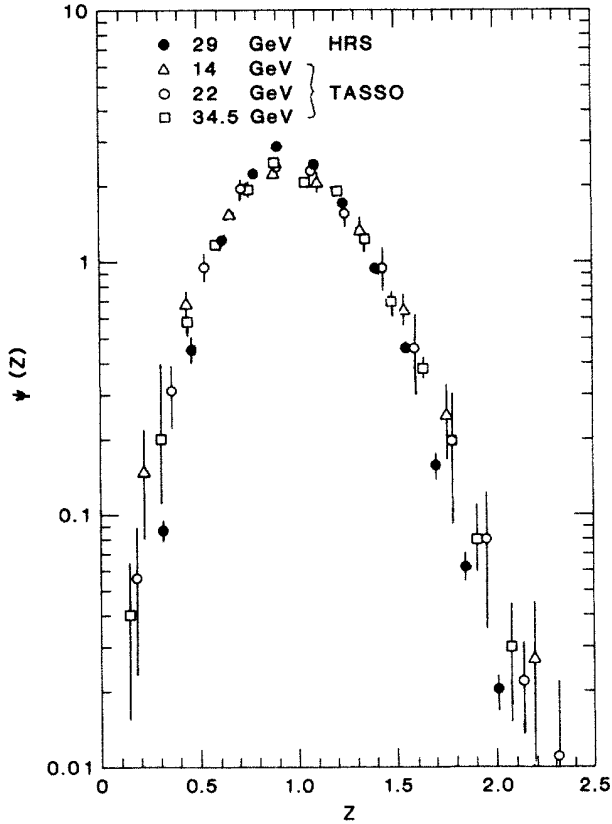


FIG. 8. Charged-particle multiplicity distribution for  $e^+e^-$  annihilation at 29 GeV in KNO form compared to measurements of the TASSO Collaboration.

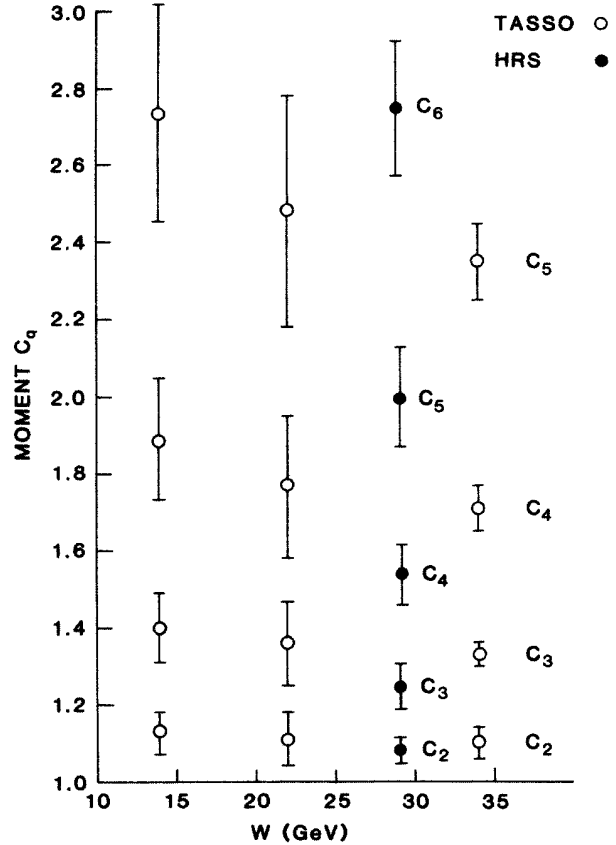


FIG. 9. Moments of the multiplicity distribution for the HRS data at  $W=29$  GeV compared to the TASSO results.

earlier experiments are large, and the previous authors also used MC estimates for the low multiplicities, whereas we use the data themselves assuming independent jet fragmentation. The large integrated luminosity of the HRS experiment allows the data sample to be restricted to events in the central region of the detector so the higher multiplicities should be more reliably measured.

Figure 9 shows the center-of-mass energy dependence of the moments of the complete distribution ( $C_q$ ) for our data and for the TASSO experiment.<sup>4</sup> The errors shown for the HRS results include the systematic uncertainties, whereas for the TASSO data, only the statistical errors are used. The systematic uncertainty on  $\langle n \rangle$  dominates the errors on the  $C_q$  moments listed in Table III. The

higher moments of the HRS distribution are smaller than those from the TASSO data, consistent with the narrower KNO distribution seen in Fig. 8.

The data of Table I have been fit to the negative binomial of Eq. (5) and to the gamma distribution of Eq. (9), with results listed in Table II. The NB gives a good fit in all cases. Including the systematic errors, the  $\chi^2$  per degree of freedom is about 0.5. Since the HRS data give an almost Poissonian distribution (for which  $k = \infty$ ), the fitted  $k$  values are large. The values of the  $C_q$  moments for the NB fits<sup>31</sup> are given in Table III. In all cases, the values calculated from the NB fits are in good agreement with those directly measured. Similar fits<sup>32</sup> to the TASSO data gave  $k$  values of 62 at 14 GeV, 44 at  $W=22$  GeV,

TABLE III. Multiplicity moments.

Moment	Inclusive sample				Two-jet sample			
	Whole event		Single jet		Whole event		Single jet	
	Expt	NB	Expt	NB	Expt	NB	Expt	NB
$C_2$	$1.08 \pm 0.04$	1.08	$1.16 \pm 0.04$	1.16	$1.08 \pm 0.04$	1.08	$1.15 \pm 0.04$	1.16
$C_3$	$1.25 \pm 0.06$	1.25	$1.50 \pm 0.07$	1.50	$1.24 \pm 0.06$	1.25	$1.49 \pm 0.07$	1.51
$C_4$	$1.54 \pm 0.08$	1.54	$2.13 \pm 0.11$	2.12	$1.51 \pm 0.08$	1.53	$2.09 \pm 0.10$	2.15
$C_5$	$2.00 \pm 0.12$	1.98	$3.27 \pm 0.18$	3.25	$1.93 \pm 0.12$	1.99	$3.18 \pm 0.18$	3.33
$C_6$	$2.75 \pm 0.18$		$5.38 \pm 0.35$		$2.61 \pm 0.18$		$5.19 \pm 0.34$	

and 35 at  $W=34$  GeV, which are smaller than  $k=259$  measured for our inclusive data sample. The GD has only one free parameter and the fits, which are less good than the NB, give smaller  $K$  values that are close to  $\langle n \rangle$  as seen in Table II.

Figure 10 shows the HRS data, together with the best-fit curves to the negative-binomial expression of Eqs. (5). Similar fits to the gamma distribution of Eq. (9) can be seen in Fig. 11. In these figures, the errors plotted are the quadratic sum of the statistical and systematic uncertainties.

Many explanations of the origin of the NB and GD have been given.<sup>33</sup> The NB, defined for integral values of  $n$ , can be derived assuming that the final-state particles obey Bose-Einstein statistics. According to these ideas,  $K$  can be thought of as the number of identical emitters or cells in phase space. An alternative interpretation<sup>34</sup> is that the emission of more particles is stimulated by the bosons already present in a given cell, and  $1/k$  represents the average fraction of existing particles that stimulate the emission of additional particles. Expressions giving similar KNO shapes can also be derived from a generating function that describes the QCD branching processes at the parton level.<sup>35</sup> The one-parameter GD also gives a reasonable representation of the results, although it falls

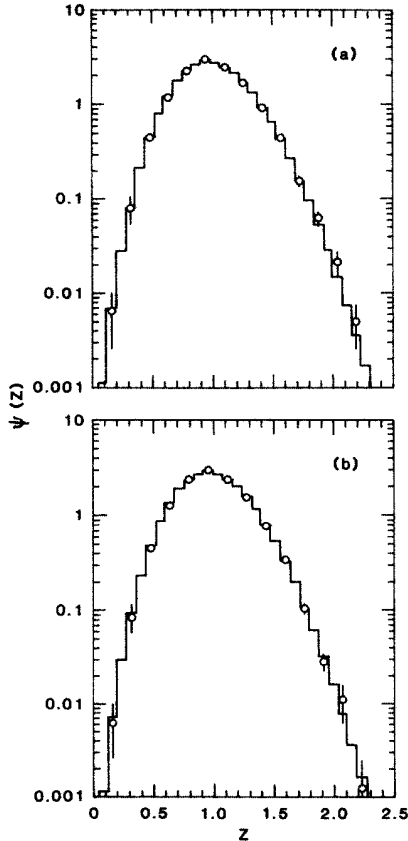


FIG. 10. Charged-particle multiplicity distributions for  $e^+e^-$  annihilation at 29 GeV compared to the negative-binomial distribution: (a) inclusive data set, (b) two-jet data set.

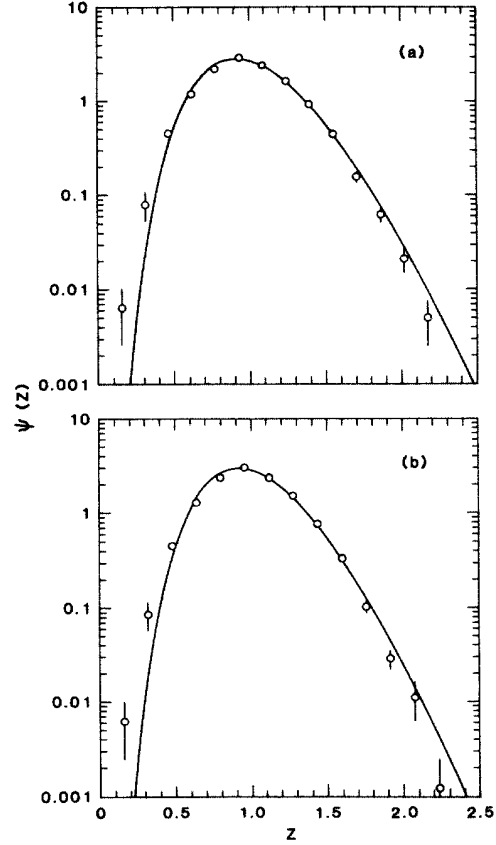


FIG. 11. Charged-particle multiplicity distributions for  $e^+e^-$  annihilation at 29 GeV compared to the gamma distribution: (a) inclusive data set, (b) two-jet data set.

below the data at the lowest  $n$  values. There is, at present, no fundamental understanding of these parametrizations, and so neither expression can be considered to be the more fundamental, although, since the multiplicities are by their very nature discrete, the NB is perhaps more natural.

Giovannini and Van Hove<sup>34</sup> also show that the multiplicity distributions, when interpreted with the NB distribution, can be used to estimate the mean multiplicity of intermediate clusters,  $\langle n \rangle_c$ , assuming that the charged particles result from cluster decay. The result is

$$\langle n \rangle_c = \frac{B}{B-1} \frac{1}{\ln(1-B)}, \quad (17)$$

where  $B = \langle n \rangle / (\langle n \rangle + k)$ . The fits to the HRS data given in Table II result in a cluster multiplicity of one in agreement with the idea of independent emission of single particles.

Multiplicity distributions have been measured for a number of hadronic interactions and over a large energy range.<sup>24</sup> As an example, in Fig. 12 the partial prong cross sections  $\sigma_n$  for this experiment, normalized to the total cross section of 0.39 nb, are compared to nondiffractive  $pp$  data at  $W=19.6$  GeV (Ref. 36) having a  $\langle n \rangle$  value of  $8.56 \pm 0.12$ . It is clear that the hadronic data have a shape quite different from the  $e^+e^-$  results, with many more

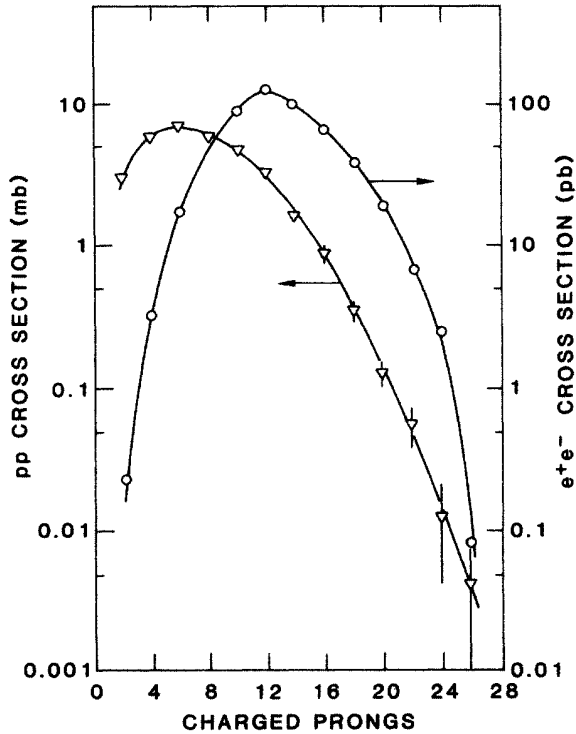


FIG. 12. Comparison of the partial cross sections for  $e^+e^-$  annihilation at  $W=29$  GeV (scale on right) with  $pp$  nondiffractive scattering at  $W=19.6$  GeV (scale on left).

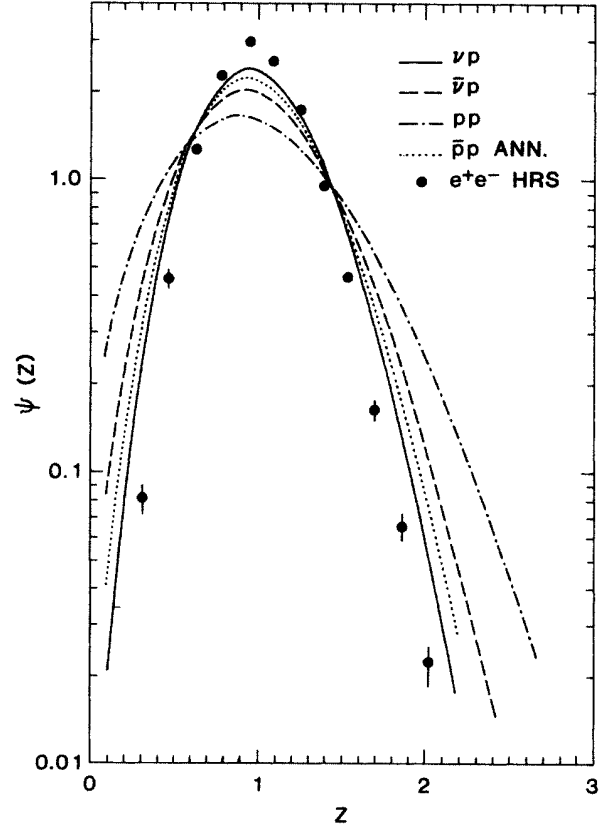


FIG. 13. Comparison of multiplicity distribution for  $e^+e^-$  annihilation at 29 GeV in KNO form with fits to data from  $p\bar{p}$  annihilation as well as  $pp$  interactions and neutrino scattering.

events having high prong numbers compared to the mean.

The multiplicity distribution for  $p\bar{p}$  annihilation at  $W$  values of a few GeV are much narrower than the  $pp$  results. They are characterized by negative  $f_2^{--}$  values, whereas the  $pp$  data have this correlation coefficient starting negative but becoming strongly positive as  $W$  is increased to the energy range of 20–60 GeV. This can be seen in Fig. 13, where the multiplicity distribution of the present experiment is compared to fits of data from the other reaction using the KNO form. The  $pp$  results are clearly wider than the fits to the  $(\nu p, \bar{\nu} p)$  and the  $p\bar{p}$  annihilation results. However, our  $e^+e^-$  data points give a distribution that is still narrower.

These qualitative observations have been interpreted in an appealing geometrical picture<sup>37</sup> in which hadronic reactions are considered to be a superposition of many collisions with different impact parameters. The central collisions give higher multiplicities and a narrow KNO distribution, more akin to the  $e^+e^-$  results, whereas the more peripheral collisions populate the lower multiplicities. The  $p\bar{p}$  annihilation process is predominantly central and so has a distribution closer to the  $e^+e^-$  results. The lepton-scattering reactions are pointlike, but they give rise to a final state with a quark and a diquark. Since diquark fragmentation<sup>27,28</sup> gives a higher  $\langle n \rangle$  than for the quark, this leads to a result intermediate between the  $e^+e^-$  and  $pp$  data.

A somewhat related discussion has been given by Chou and Yang<sup>38</sup> who consider that the annihilation process in

a given angular momentum state is stochastic, which leads to a Poissonian multiplicity distribution. Since only  $l=0$  and  $l=1$  are allowed for  $e^+e^-$  annihilation through a one-photon intermediate state, the  $e^+e^-$  multiplicity distribution should be simple, whereas for the highest-energy hadronic collisions  $l$  values up to several thousand are possible. These ideas, which are consistent with the our data, predict that KNO scaling will not hold for  $e^+e^-$  annihilation. These authors specifically consider  $e^+e^-$  annihilation leading to two jets but, as is clear from Table I, the differences between the inclusive sample and the two-jet data sample are small. Data of similar precision to the present measurements, but at higher energies, are needed to check this suggestion.

An alternative interpretation has been given by Carruthers and Shih<sup>39</sup> in which the multiplicity distribution is considered to arise from emission by a small number ( $k$ ) of cells. As we have discussed, such a picture leads to the negative-binomial expression. If there is a coherent component to the emissions, then the KNO distribution can be narrow, whereas an incoherent sum of emitters leads to a broader distribution. This is similar to the situation of a laser operating above or below threshold.

Strong KNO violations in  $p\bar{p}$  interactions have been seen at the very high energies of the CERN collider.<sup>40</sup> Many more high-multiplicity events are observed than would be predicted on the basis of the lower-energy data.

The NB expression gives a good representation of all of the high-energy  $pp$  data as well as the 540-GeV  $p\bar{p}$  results.<sup>41</sup> The fits in the  $W$  range from 10 to 100 GeV show an approximate constancy of the sum  $1/\langle n \rangle + 1/k$ , and so a constant second moment,<sup>31</sup> as well as approximately constant higher moments. In this interpretation, the observed KNO scaling in the energy range up to 60 GeV would be accidental.

Another explanation of the 540-GeV data involves the suggestion<sup>42</sup> that energy-momentum conservation strongly influences the multiplicity distributions observed at the lower energies, when the data are selected in the full rapidity range. According to this idea, the KNO distribution in the region of the rapidity plateau should be nearly free of kinematical constraints, and so give a more direct measure of the production process. The KNO distribution in restricted pseudorapidity intervals for the CERN  $p\bar{p}$  experiment<sup>41,43</sup> is indeed observed to be wider than that for the inclusive sample. This is also the case for the HRS  $e^+e^-$  data selected in this same way, as is described in a separate publication.<sup>44</sup> The NB form fits all of the HRS  $e^+e^-$  data in restricted rapidity spans, with a  $k$  value falling from the large number given in Table II, for the unrestricted data, and leveling out for the central rapidity region with  $k$  values ranging from 4 to 7.

#### VARIATION OF MEAN MULTIPLICITY WITH EVENT SHAPE

The mean charged multiplicity as a function of the event sphericity is shown in Fig. 14. The sharp rise at low

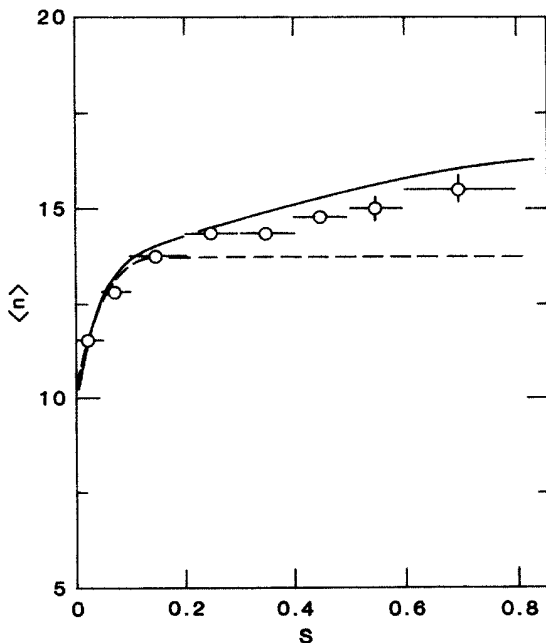


FIG. 14. Mean charged multiplicity as a function of event sphericity,  $S$ , for  $e^+e^-$  annihilation at 29 GeV. The lines show the Lund Monte Carlo prediction for the complete event sample (solid curve) and for the events with the hard-gluon radiation removed (dashed curve).

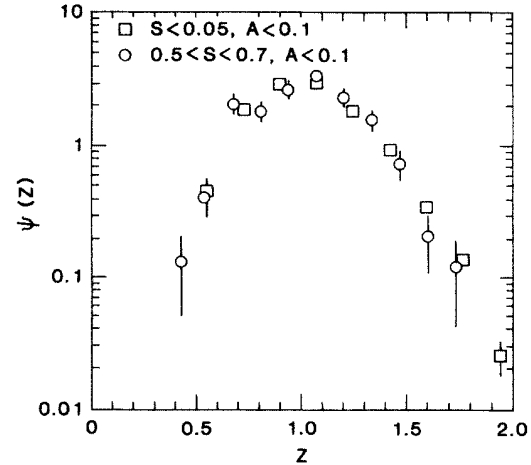


FIG. 15. Comparison of KNO distribution for low-sphericity ( $S < 0.05$ ) and high-sphericity ( $0.5 < S < 0.7$ ) events in  $e^+e^-$  annihilation at 29 GeV.

sphericity comes about because events with low prong numbers give low  $S$  values when the sphericity is defined from the charged particles alone. The slower rise, amounting to about 20% in the higher sphericity region, is the effect of hard-gluon radiation. The full line, which is in qualitative agreement with the data, shows the prediction of the MC program. If hard-gluon emission is suppressed in the MC event generation, then no such rise is predicted, as seen by the dashed line. The events at high sphericity are predominantly of the three-jet topology.

The rise of  $\langle n \rangle$  with sphericity for  $S < 0.2$  agrees with the observations of the PLUTO Collaboration.<sup>5</sup> The increase of  $\langle n \rangle$  for  $S > 0.2$ , due to hard-gluon radiation, was not previously observed. Figure 15 shows the KNO distribution for low- ( $S < 0.05$ ) and high- ( $0.5 < S < 0.7$ ) sphericity data; within errors the distributions scale, even though the events tend to come from different final states at the parton level.

In a separate study<sup>45</sup> we have isolated a sample of three-fold symmetric three-jet events in which the angle between each pair of jets in the event is between  $100^\circ$  and  $140^\circ$ . This sample, which contains 276 events, has  $\langle n \rangle = 16.3 \pm 0.3 \pm 0.7$  and  $D_2 = 4.2 \pm 0.5 \pm 0.3$ . If the events result from the symmetric  $q\bar{q}g$  partonic state and the gluon splits into a  $q'\bar{q}'$ , then in the Lund string picture, the mean charged multiplicity should just be given by twice that of the two strings connecting the  $q\bar{q}'$  and  $q'\bar{q}$  quarks whose  $W$  values can be calculated. Such a model predicts  $\langle n \rangle = 16.6$  using the energy variation of  $\langle n \rangle$  given in Fig. 4, in good agreement with the measurement.

#### SINGLE-JET MULTIPLICITIES

Most of the  $e^+e^-$  annihilation events result from the production of two back-to-back jets, which are interpreted as coming from the  $e^+e^- \rightarrow q\bar{q}$  reaction. In order to study individual quark fragmentation, we have separated all the events into two jets, assigning the charged particles in a given event to one or the other jet, according to which

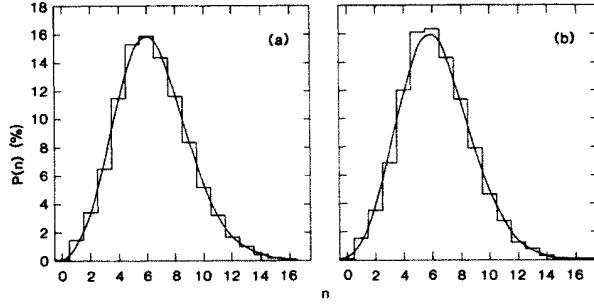


FIG. 16. Charged-particle multiplicity measurements (histogram) for single jets compared to the line that connects points on a Poisson distribution with the same mean value for (a) inclusive data sample and (b) two-jet data sample.

detector hemisphere they populate; the equator is chosen to be the plane perpendicular to the thrust axis.

For single jets selected in this way, the mean charged multiplicity is  $\langle n \rangle = 6.43 \pm 0.02 \pm 0.15$ , the dispersion is  $\mathcal{D}_2 = 2.55 \pm 0.02 \pm 0.13$ , and the ratio  $\langle n \rangle / \mathcal{D}_2$  per jet is  $2.52 \pm 0.13$ , where the error is dominated by the systematics. This value is lower by the square root of 2 than the value  $\langle n \rangle / D_2 = 3.51 \pm 0.03$ , obtained for the complete event; i.e., the normalized spread of the multiplicity distribution per jet is a factor of root 2 narrower than for the whole event, as expected if the multiplicities in the two jets are uncorrelated.

Figures 16(a) and 16(b) show the single-jet multiplicity distributions for the inclusive and two-jet data samples. The curves show the Poisson distribution of Eq. (7), calculated for the corresponding mean values. Again, as was the case for the prong distributions for the whole event shown in Fig. 6, the simple Poisson shapes give a good representation of the measurements. If the multiplicity distribution for the complete events is an incoherent sum of the individual Poissonian jets, then the resulting multi-

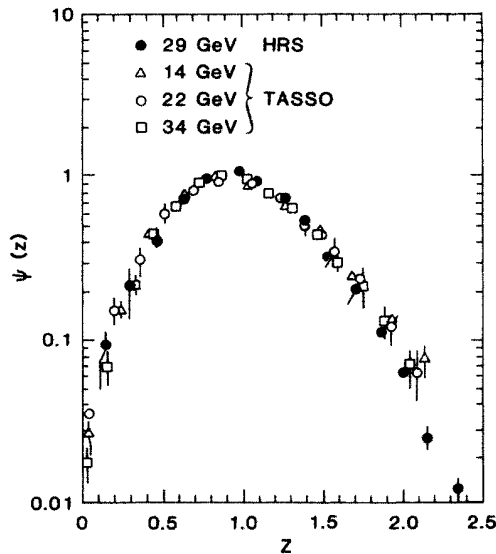


FIG. 17. Single-jet multiplicity distribution for the inclusive event sample in KNO form compared to the measurements of the TASSO Collaboration.

plicity will be almost Poissonian, as is observed in Fig. 6.

In Fig. 17 the singlet-jet KNO distribution for the inclusive data set is compared with results from the TASSO experiment<sup>4</sup> at  $W$  values of 14, 22, and 34 GeV. The agreement among the data points is quite good, so that approximate KNO scaling also holds for the single-jet multiplicities.

The single-jet multiplicity distributions in KNO form are compared to the NB fits in Fig. 18 and to the GD fits in Fig. 19. The errors shown are the quadratic sum of the statistical and systematic uncertainties. Again the NB form represents the data very well, whereas the GD fits are not as good. The resulting values of  $k$  and  $K$  are given in Table II. The moments of the single-jet distributions are given in Table III.

### JET-JET MULTIPLICITY CORRELATIONS

The comparison of the widths of the single-jet and complete-event multiplicity distributions support the idea of independent jet fragmentation. This can be directly checked by measuring the multiplicity correlation between the two jet hemispheres.

The mean multiplicity in one jet ( $F$ ) is compared to the number of charged particles in the second jet ( $B$ ) in Fig. 20(a). There is clearly no strong correlation between the

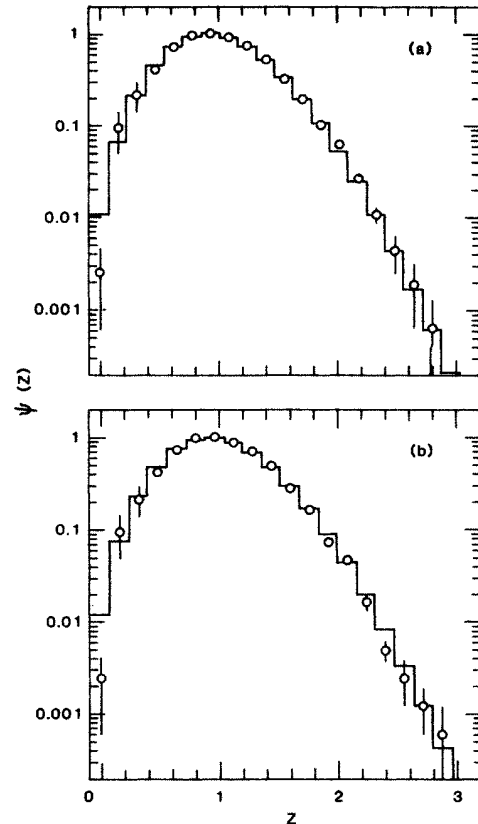


FIG. 18. Single-jet charged-particle multiplicity distributions for  $e^+e^-$  annihilation at 29 GeV compared to the negative-binomial distribution: (a) inclusive data set; (b) two-jet data set.

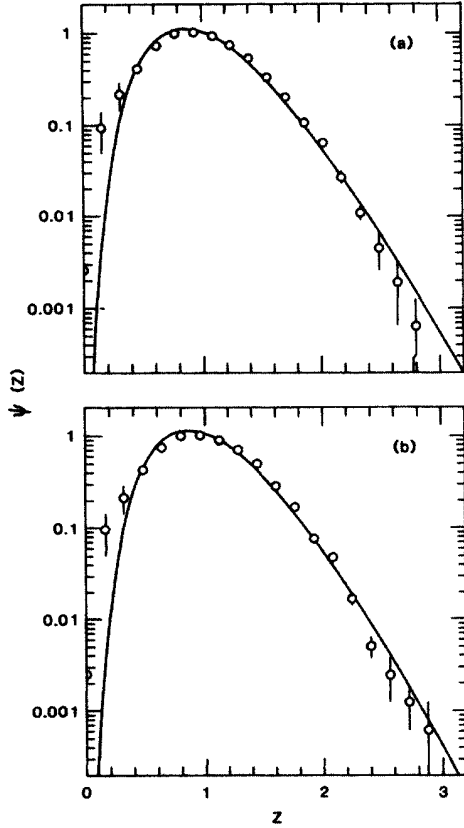


FIG. 19. Single-jet charged-particle multiplicity distributions for  $e^+e^-$  annihilation at 29 GeV compared to the gamma distribution: (a) inclusive data set; (b) two-jet data set.

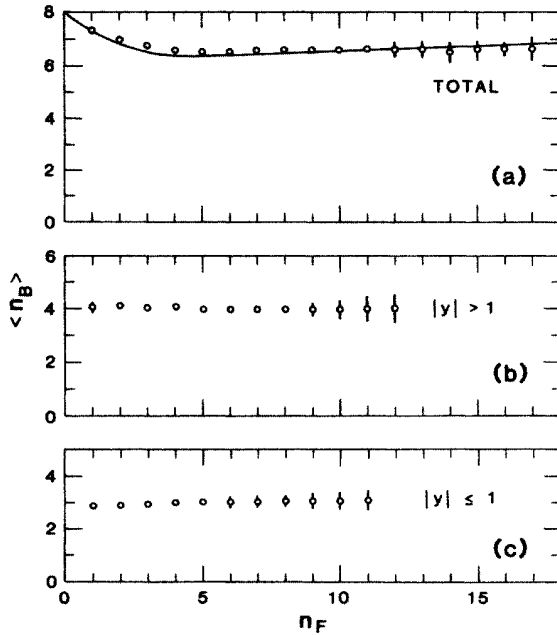


FIG. 20. Forward-backward multiplicity correlations for (a) full rapidity span, (b) tracks with  $|Y| \le 1.0$  removed, (c) tracks in the region  $|Y| \le 1.0$ . The errors shown are dominated by the systematic uncertainties.

multiplicities in the two hemispheres. While these results are corrected for inefficiencies and detector smearing effects, they are not corrected for the biases at low multiplicities introduced by the selection criteria ( $m \geq 5$ ), since this correction was made assuming no jet-jet multiplicity correlation, an assertion that we are now testing. This cut is responsible for the small correlation effect observed for low multiplicities in the  $B$  hemisphere. The line shows the results of a simple calculation using the measured  $\langle n \rangle$  values for  $(u,d,s)$ ,  $c$ , and  $b$  quarks (Ref. 7), as well as the effect of the cut at  $m < 5$ .

The analysis has been repeated [Fig. 20(b)] with the central rapidity region removed ( $|Y| \leq 1$ ). This selection is made because of a possible bias coming from particles near  $Y=0$ , whose jet assignment could be affected by the uncertainties of the thrust axis direction. Such particles are often of low momentum and so are not reconstructed by the spectrometer with full efficiency. In addition, this selection removes any correlation that could result from the decay of a centrally produced heavy cluster whose decay products could fall in both hemispheres, and so give an  $F$ - $B$  correlation.

If the data of Fig. 20 are fit to the linear relationship

$$\langle n_B \rangle = a + b n_F, \quad (18)$$

the following values are obtained:<sup>46,47</sup>  $b = -0.001 \pm 0.015$  for the unselected data with  $n_F \geq 6$  [Fig. 20(a)];  $b = +0.002 \pm 0.006$  for the data with  $|Y| > 1$  [Fig. 20(b)]; and  $b = +0.036 \pm 0.011$  for the data with  $|Y| < 1$  [Fig. 20(c)]. The errors are completely dominated by the systematic uncertainties. If the forward-backward correlation function  $R$  is defined as

$$R = \frac{\langle n_F n_B \rangle - \langle n_F \rangle \langle n_B \rangle}{\mathcal{D}_F \mathcal{D}_B}, \quad (19)$$

and

$$D^2 = \mathcal{D}_F^2 + \mathcal{D}_B^2 + 2(\langle n_F n_B \rangle - \langle n_F \rangle \langle n_B \rangle),$$

then since  $\mathcal{D}_B = \mathcal{D}_F = \mathcal{D}_2$ , the following relationship results:<sup>48</sup>

$$\mathcal{D}_2 = \frac{D_2}{\sqrt{2(1+b)}}. \quad (20)$$

The values for the single-jet dispersions ( $\mathcal{D}_2$ ) and those for the whole event ( $D_2$ ) given in Table II, yield  $b$  values of  $0.04 \pm 0.02 \pm 0.10$  for the inclusive sample and  $0.01 \pm 0.2 \pm 0.10$  for the two-jet sample, in agreement with the direct measurement.

These data, which establish independent jet fragmentation for  $e^+e^-$  annihilation may be contrasted with the results of  $pp$  collisions at the ISR (Ref. 49) and with the high-energy  $\bar{p}p$  data,<sup>50</sup> which show a strong positive  $F$ - $B$  correlation with a slope increasing with energy from  $b=0.2$  at 20 GeV to  $b=0.54 \pm 0.01$  at 540 GeV.

The observed broad multiplicity distribution and the strong  $F$ - $B$  correlations observed in the hadronic data have been interpreted with a dual model in which  $pp$  scattering goes by the exchange of two chains.<sup>48,51</sup> The results have also been fitted in models with random emission of clusters along the rapidity axis.<sup>50,52</sup>

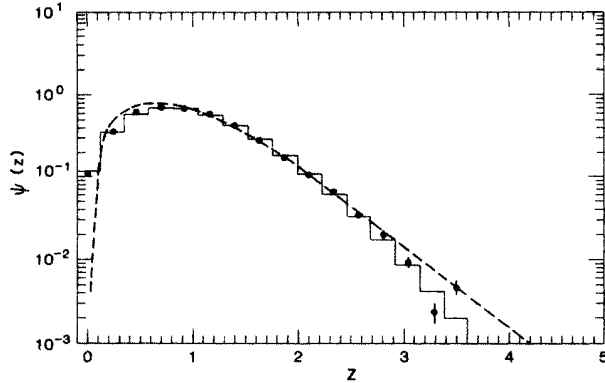


FIG. 21. Multiplicity distribution in KNO form for the inclusive data sample with  $|Y| < 1.0$ . The histogram shows the best fit of the data to the negative binomial; the dashed line gives the gamma distribution with  $K=3$ .

According to these ideas, the large (small) value of  $b$  and the broad (narrow) KNO multiplicity distribution are intimately related. In this respect, it is interesting to note that for  $e^+e^-$  data selected in the central region of rapidity  $|Y| < 1$  there is at best a very small  $F$ - $B$  correlation as seen in Fig. 20(c), but the multiplicity distribution with this selection, shown in Fig. 21, is characterized by  $\langle n \rangle = 4.82 \pm 0.02$  and a  $k$  value for the NB fit of  $6.99 \pm 0.05$  (statistical errors). The dashed curve in Fig. 21 shows, for illustration, the gamma distribution for  $K=3$ ,  $\psi(Z) = 13.5 Z^2 e^{-3Z}$ . These results support the suggestion of Bialas and Hayot<sup>41</sup> that the shape of the multiplicity distribution in the full rapidity span is constrained by energy and momentum conservation. However, in this case, the agreement of the unselected data with a Poisson distribution would be accidental, which is remarkable.

### RAPIDITY DISTRIBUTIONS

The corrected rapidity distribution along the thrust axis is shown in Fig. 22(a). The distribution has a flat plateau but with a shallow dip near  $|Y|=0$ . All particles are assigned the pion mass in calculating the rapidity and so any heavier particle is shifted to larger  $|Y|$  values. The central dip still remains, however, after correcting for this effect.<sup>1</sup> Figure 22 also shows the rapidity distributions for three different multiplicity selections [22(b)] low ( $n \leq 8$ ), [22(c)] medium ( $10 \leq n \leq 12$ ) and [22(d)] high ( $n \geq 14$ ). As  $n$  increases, the distributions become narrower and the central dip is enhanced. This is consistent with the observation that much of the peaking near  $|Y| \simeq 1.2$  results from hard-gluon emission and from particles coming from the decay of  $D$  and  $B$  mesons containing the  $c$  and  $b$  quarks. Such events have a higher than average multiplicity.<sup>7</sup> The data of Fig. 22 also show a narrowing of the multiplicity distributions as  $n$  increases. This result may be another effect of energy and momentum conservation.

### CONCLUSIONS

The charged-particle multiplicity distributions and forward-backward correlations presented in this paper are

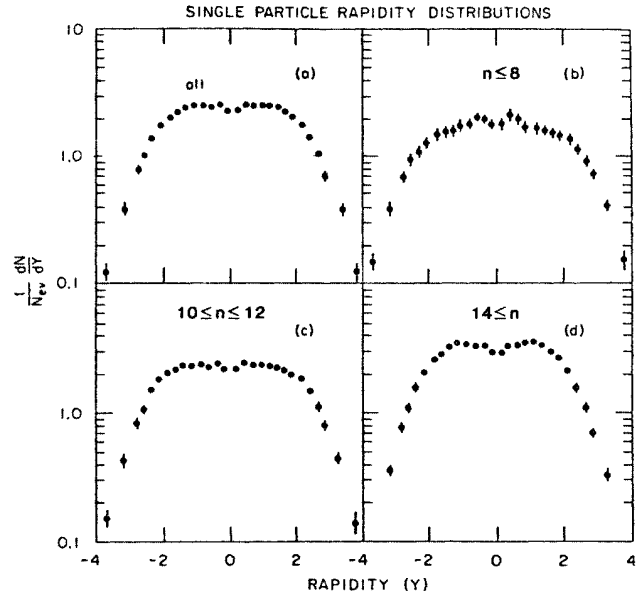


FIG. 22. Rapidity distributions relative to the thrust axis. (a) all events, (b)  $n \leq 8$ , (c)  $10 \leq n \leq 12$ , and (d)  $n \geq 14$ .

in agreement with the simplest picture of the  $e^+e^-$  annihilation being dominated by  $e^+e^- \rightarrow q\bar{q}$  with the materialization of the  $q$  and  $\bar{q}$  into hadrons proceeding independently. The detailed results are completely different from the hadronic data showing that the similarities between data from the two reactions pointed out by Basile *et al.*<sup>10</sup> are only superficial. The Poissonian shape of the multiplicity distribution and the lack of correlation between  $\langle n_F \rangle$  and  $n_B$  suggests the direct and independent production of hadrons. Such a picture must be reconciled with the known strong resonance production in  $e^+e^-$  annihilation and with the observed rapidity correlations<sup>47,53</sup> which are not in agreement with this simple picture. The present  $e^+e^-$  multiplicity results also cast doubt on the long-held belief that the clusters needed to interpret the hadronic data are to be identified with resonances.

Data on  $e^+e^-$  annihilation at other energies are needed to see if the multiplicity distributions remain Poissonian. At the present energies, more detailed studies, both of the multiplicities in restricted regions of the phase space and of correlations, are needed to elucidate the interplay between global measurements such as multiplicity and the detailed nature of the hadronization processes.

### ACKNOWLEDGMENTS

We thank P. Carruthers, B. Durand, V. Khoze, L. Van Hove, and A. Wroblewski for interesting discussions and correspondence on the meaning of multiplicity distributions. This work was supported in part by the U.S. Department of Energy under Contracts Nos. W-31-109-Eng-38, DE-AC02-76ER01112, DE-AC03-76SF00098, DE-AC02-76ER01428, and DE-AC02-84ER40125. We thank the PEP operations group for providing the luminosity on which these results are based.

- (a) Present address: SLAC, Stanford, CA 94305.  
 (b) Present address: SRI International, Menlo Park, CA 94025.  
 (c) Present address: Lockheed Missiles and Space Co., Sunnyvale, CA 94086.  
 (d) Present address: University of Wisconsin, Madison, WI 53706.  
 (e) Present address: Laboratory for Nuclear Studies, Cornell University, Ithaca, NY 14853.  
 (f) Permanent address: INFN, Pisa, Italy.  
 (g) Present address: CERN, 1211 Geneva 23, Switzerland.  
 (h) Present address: Brandeis University, Waltham, MA 02254.  
 (i) Present address: ETH, Zurich, Switzerland.  
<sup>1</sup>D. Bender *et al.*, Phys. Rev. D **31**, 1 (1985).  
<sup>2</sup>JADE Collaboration, W. Bartel *et al.*, Z. Phys. C **9**, 315 (1981); **20**, 187 (1983).  
<sup>3</sup>LENA Collaboration, B. Niczyporuk *et al.*, Z. Phys. C **9**, 1 (1981).  
<sup>4</sup>TASSO Collaboration, M. Althoff *et al.*, Z. Phys. C **22**, 307 (1984).  
<sup>5</sup>PLUTO Collaboration, Ch. Berger *et al.*, Phys. Lett. **81B**, 410 (1979); **95B**, 313 (1980); Z. Phys. C **12**, 297 (1982).  
<sup>6</sup>Mark II Collaboration, J. L. Seigrist *et al.*, Phys. Rev. D **26**, 969 (1982).  
<sup>7</sup>M. Althoff *et al.*, Phys. Lett. **135B**, 243 (1984); M. Sakuda *et al.*, *ibid.* **152B**, 399 (1985); P. Kesten *et al.*, *ibid.* **161B**, 412 (1985).  
<sup>8</sup>P. Bagnaia *et al.*, Phys. Lett. **144B**, 291 (1984).  
<sup>9</sup>M. Derrick *et al.*, Phys. Lett. **165B**, 449 (1985).  
<sup>10</sup>M. Basile *et al.* Nuovo Cimento **79A**, 1 (1984), and references cited therein.  
<sup>11</sup>Z. Koba, M. B. Nielsen, and P. Olesen, Nucl. Phys. **B40**, 317 (1972).  
<sup>12</sup>D. Bender *et al.*, Phys. Rev. D **30**, 515 (1984).  
<sup>13</sup>B. Andersson *et al.*, Z. Phys. C **1**, 105 (1978).  
<sup>14</sup>R. D. Field and R. P. Feynman, Nucl. Phys. **B136**, 1 (1978).  
<sup>15</sup>M. Derrick *et al.*, Phys. Lett. **146B**, 261 (1984).  
<sup>16</sup>M. Derrick *et al.*, Phys. Rev. D **31**, 2352 (1985); K. K. Gan *et al.*, Phys. Lett. **153B**, 116 (1985); M. Derrick *et al.*, *ibid.* **166B**, 463 (1986).  
<sup>17</sup>M. Derrick *et al.*, Report No. PU-85-537 (unpublished).  
<sup>18</sup>P. Baringer *et al.*, Phys. Rev. Lett. **56**, 1346 (1986).  
<sup>19</sup>ADONE Collaboration, C. Bacci *et al.*, Phys. Lett. **86B**, 234 (1979).  
<sup>20</sup>E. Fermi, Prog. Theor. Phys. **5**, 570 (1950).  
<sup>21</sup>R. P. Feynman, Phys. Rev. Lett. **23**, 1415 (1969).  
<sup>22</sup>A. Basetto *et al.*, Phys. Lett. **83B**, 207 (1979).  
<sup>23</sup>W. Fourmanski *et al.*, Nucl. Phys. **B155**, 253 (1979).  
<sup>24</sup>A. Wroblewski, Acta. Phys. Pol. **B15**, 785 (1984) gives a compilation of multiplicity measurements in hadronic collisions. See also E. Albini *et al.*, Nuovo Cimento **32A**, 101 (1976).  
<sup>25</sup>W. Thome *et al.*, Nucl. Phys. **B129**, 365 (1977) ( $pp$ ).  
<sup>26</sup>K. Alpgard *et al.*, Phys. Lett. **107B**, 315 (1981); **115B**, 71 (1982), ( $\bar{p}p$ ).  
<sup>27</sup>H. Grassler *et al.*, Nucl. Phys. **B223**, 269 (1983) ( $\nu p, \bar{\nu} p$ ).  
<sup>28</sup>M. Arneodo *et al.*, Nucl. Phys. **B258**, 249 (1985) ( $\mu p$ ).  
<sup>29</sup>J. G. Rushbrooke and B. R. Webber, Phys. Rep. **44**, 1 (1978), ( $\bar{p}p$  annihilation).  
<sup>30</sup>M. Derrick *et al.*, Phys. Lett. **146B**, 261 (1984); **158B**, 519 (1985).  
<sup>31</sup>The first five moments are given by

$$C_1 = 1,$$

$$C_2 = 1 + \frac{1}{\langle n \rangle} + \frac{1}{k},$$

$$C_3 = \left[ 1 + \frac{1}{k} \right] \left[ 1 + \frac{2}{k} \right] + \frac{3}{\langle n \rangle} \left[ 1 + \frac{1}{k} \right] + \frac{1}{\langle n \rangle^2},$$

$$C_4 = \left[ 1 + \frac{1}{k} \right] \left[ 1 + \frac{2}{k} \right] \left[ 1 + \frac{3}{k} \right] + \frac{6}{\langle n \rangle} \left[ 1 + \frac{1}{k} \right] \left[ 1 + \frac{2}{k} \right] + \frac{7}{\langle n \rangle^2} \left[ 1 + \frac{1}{k} \right] + \frac{1}{\langle n \rangle^3},$$

$$C_5 = \left[ 1 + \frac{1}{k} \right] \left[ 1 + \frac{2}{k} \right] \left[ 1 + \frac{3}{k} \right] \left[ 1 + \frac{4}{k} \right] + \frac{10}{\langle n \rangle} \left[ 1 + \frac{1}{k} \right] \left[ 1 + \frac{2}{k} \right] \left[ 1 + \frac{3}{k} \right] + \frac{25}{\langle n \rangle^2} \left[ 1 + \frac{1}{k} \right] \left[ 1 + \frac{2}{k} \right] + \frac{15}{\langle n \rangle^3} \left[ 1 + \frac{1}{k} \right] + \frac{1}{\langle n \rangle^4}.$$

- <sup>32</sup>C. K. Chew and Y. K. Lim, ICTP Report No. IC/85/63 1985 (unpublished).  
<sup>33</sup>A. Giovannini, Nuovo Cimento **15A**, 543 (1973); W. J. Knox, Phys. Rev. D **10**, 65 (1974); P. Carruthers and C. C. Shih, Phys. Lett. **127B**, 242 (1983).  
<sup>34</sup>A. Giovannini and L. Van Hove, Z. Phys. C **90**, 391 (1986).  
<sup>35</sup>B. Durand and S. D. Ellis, in *Proceedings of the Summer Study on the Design and Utilization of the Superconducting Super Collider*, Snowmass, Colorado, 1984, edited by J. Morfin and R. Donaldson (Division of Particles and Fields of the American Physical Society, New York, 1985), p. 234.  
<sup>36</sup>S. J. Barish *et al.*, Phys. Rev. D **9**, 2689 (1974).  
<sup>37</sup>J. Dias de Deus, Nucl. Phys. **B59**, 231 (1973); S. Barshay and Y. Yamaguchi, Phys. Lett. **51B**, 376 (1974); S. Barshay, *ibid.* **116B**, 193 (1982); S. Barshay and L. Urban, *ibid.* **150B**, 387 (1985). Barshay predicts  $\psi(Z) = \frac{81}{64} \pi^2 Z^3 \exp(-\frac{9}{10} \pi Z^2)$  as the KNO distribution for  $e^+e^-$  annihilation. This form fits the  $\bar{p}p$  data well but is wider than the  $e^+e^-$  results presented in this paper.  
<sup>38</sup>T. T. Chou and C. N. Yang, Phys. Rev. Lett. **55**, 1359 (1985). These authors [T. T. Chou, C. N. Yang, and E. Yen, *ibid.* **54**, 510 (1985)] further suggest that  $e^+e^-$  annihilation will be similar to hadronic interactions at zero impact parameter. The mean momentum per charged particle in our data is 1.3 GeV/c, which may be compared to 1.64 GeV/c estimated for central  $\bar{p}p$  collisions at 540 GeV.  
<sup>39</sup>P. Carruthers and C. C. Shih, Phys. Lett. **137B**, 425 (1984).  
<sup>40</sup>K. Alpgard *et al.*, Phys. Lett. **138B**, 304 (1984).  
<sup>41</sup>G. J. Alner *et al.*, Phys. Lett. **160B**, 199 (1985).  
<sup>42</sup>A. Bialas and F. Hayot, Phys. Rev. D **33**, 39 (1986).  
<sup>43</sup>G. J. Alner *et al.*, Phys. Lett. **160B**, 193 (1985).  
<sup>44</sup>M. Derrick *et al.*, Phys. Lett. **168B**, 299 (1986).  
<sup>45</sup>M. Derrick *et al.*, Phys. Lett. **165B**, 449 (1985).  
<sup>46</sup>H. Aihara *et al.*, Z. Phys. C **27**, 495 (1985).  
<sup>47</sup>M. Althoff *et al.*, Z. Phys. C **29**, 347 (1985).  
<sup>48</sup>K. Fialkowski and A. Kotanski, Phys. Lett. **115B**, 425 (1982); in *Multiparticle Dynamics 1984*, proceedings of the XV Symposium, Lund, Sweden, 1984, edited by G. Gustafson and C. Peterson (World Scientific, Singapore, 1984), p. 30.



<sup>49</sup>S. Uhlig *et al.*, Nucl. Phys. **B132**, 15 (1978).

<sup>50</sup>K. Alpgard *et al.*, Phys. Lett. **123B**, 361 (1983); B. Asman, Ph.D. thesis, Stockholm, 1985.

<sup>51</sup>A. Capella, U. Sukhatme, and J. Tran Than Van, Z. Phys. C **3**, 329 (1980).

<sup>52</sup>P. Carruthers and C. C. Shih, Phys. Lett. **165B**, 209 (1985).

<sup>53</sup>M. Valdata-Nappi, in *Multiparticle Dynamics 1983*, proceedings of the XIV Symposium, Lake Tahoe, 1983, edited by P. Yager and J. F. Gunion (World Scientific, Singapore, 1984), p. 75.